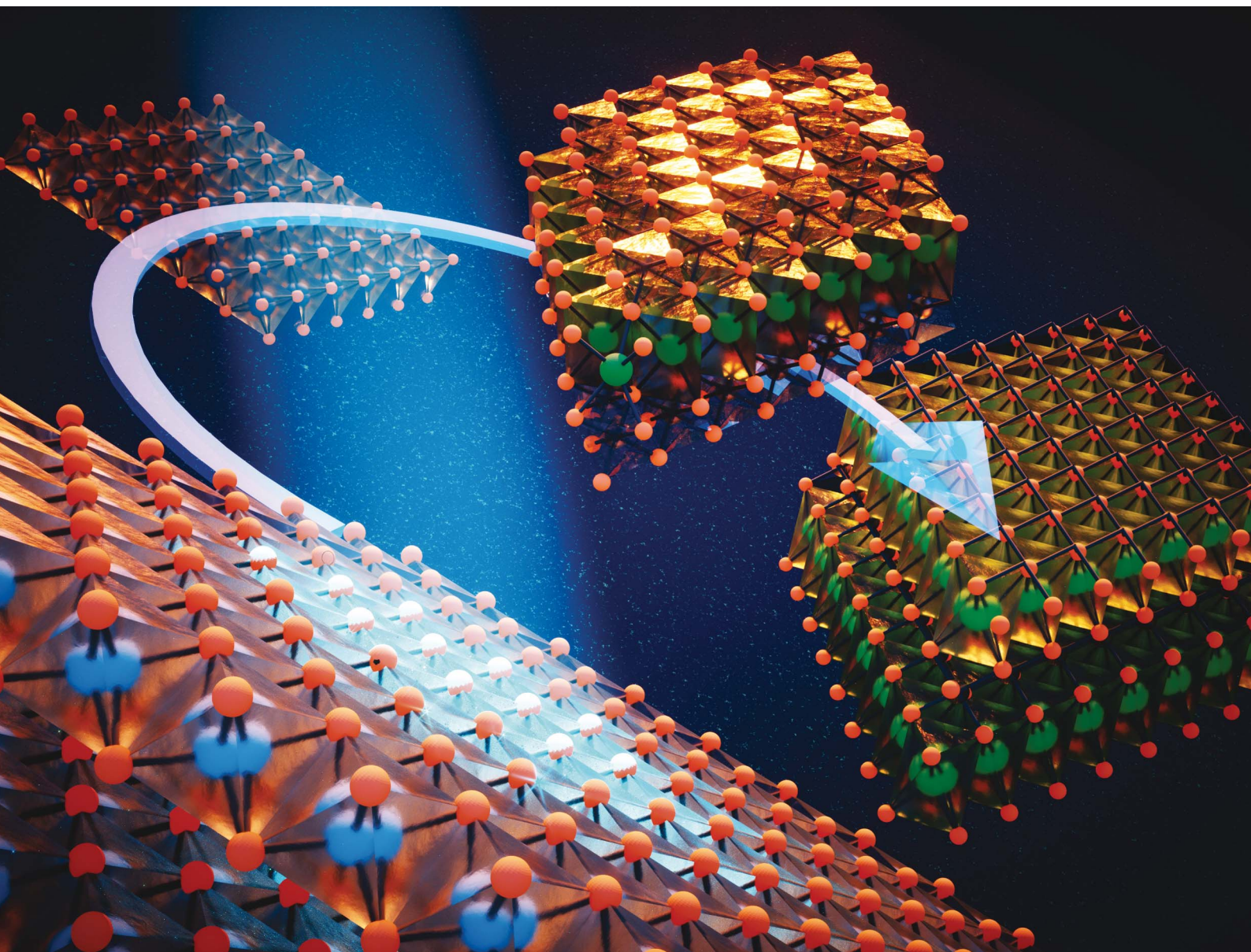


Journal of Materials Chemistry A

Materials for energy and sustainability

rsc.li/materials-a



ISSN 2050-7488

PAPER

Yu-chen Karen Chen-Wiegart *et al.*
Operando structural and chemical evolutions of TiS_2 in
Na-ion batteries

PAPER



Cite this: *J. Mater. Chem. A*, 2020, **8**, 12339

Operando structural and chemical evolutions of TiS₂ in Na-ion batteries†

Cheng-Hung Lin,^a Mehmet Topsakal,^b Ke Sun,^{ac} Jianming Bai,^d Chonghang Zhao,^a Eric Dooryhee,^d Paul Northrup,^e Hong Gan,^c Deyu Lu,^f Eli Stavitski^d and Yu-chen Karen Chen-Wiegart^{id}*^{ad}

Titanium disulfide (TiS₂) with high electric conductivity, fast rate capability, and good cycling performance is a promising candidate for electrode material in sodium (Na)-ion batteries. Despite the well-studied electrochemical behaviors of TiS₂ in Li-ion batteries, the detailed reaction mechanism of TiS₂ in Na-ion batteries is not yet fully understood due to a more complex multi-phase conversion process. In this work, reactions of TiS₂ in Na-ion batteries are investigated via a multi-modal synchrotron approach: *operando* X-ray Absorption Spectroscopy (XAS) – including X-ray Absorption Near-Edge Structure (XANES) and Extended X-ray Absorption Fine Structure (EXAFS) – and *ex situ* X-ray Powder Diffraction (XPD), coupled with computational modeling. *Operando* XANES spectra indicate that the redox reactions occur in both Ti and S during the electrochemically driven phase transformation. Multivariate Curve Resolution-Alternating Least Squares (MCR-ALS) analysis of XAS suggests that different numbers of components are involved in the lithiation and sodiation of TiS₂, with the sodiation including at least one intermediate phase in addition to the starting material and the final sodiation product. *Ex situ* XPD and Rietveld refinement further determined and quantified the unknown phases, showing that three phases, TiS₂, Na_{0.55}TiS₂, and NaTiS₂, participate in the sodiation of TiS₂. *Operando* EXAFS results show the changes in the Ti–Ti coordination number and interatomic distance. This explains the coulombic efficiency decay due to the incomplete recovery of the coordination number of Ti after cycling. Overall, this work reveals the reaction mechanism occurring in Na–TiS₂ batteries with a greater quantitative understanding of the structural evolution. By combining the multi-modal synchrotron approach and computational work, this study provides a framework for studying a broader range of electrochemically driven phase-transformation systems towards advanced energy storage and conversion applications.

Received 7th January 2020
Accepted 14th April 2020

DOI: 10.1039/d0ta00226g

rsc.li/materials-a

1. Introduction

Large-scale energy storage such as electric vehicles (EVs) and intermittent sustainable energy for electrical grids have attracted accumulating research interest and booming investment in recent years. A large research gap remains for current lithium-ion batteries (LIBs) to satisfy the demands of large-scale storage. The

battery technology continues to advance to increase energy density, stability and safety at a reduced cost. Today, cobalt/nickel-based metal oxides, such as LiCoO₂, LiNi_xCo_yMn_zO₂, and LiNi_{0.53}Co_{0.3}Al_{0.17}O₂, dominate the cathode materials in commercial lithium coin cells.¹ However, to reduce the cost and achieve a better performance,² researchers continue searching for potential alternative electrodes.

Layered transition metal dichalcogenides (MX₂; M = transition metal, X = S, Se, Te) provide another promising direction for the intercalation of host species in cathodes. Titanium disulfide (TiS₂) has been studied extensively since its kinetically favorable insertion reaction in alkali metals was reported by Whittingham in 1976.³ Because of its good electrical conductivity,⁴ higher energy density than LiCoO₂, and rapid cycling rate,⁴ TiS₂ is now considered as a strong contender in LIBs and beyond Li-ions, such as Na, K, and Mg, for application in high-power systems.^{5–7} Moreover, TiS₂ provides the possibility for incorporation with a metal lithium anode for an all-solid-state cell and acts as an absorber of Li-polysulfides in lithium-sulfur batteries to enhance cell performance.⁸

^aDepartment of Materials Science and Chemical Engineering, Stony Brook University, Stony Brook, NY 11794, USA. E-mail: Karen.Chen-Wiegart@stonybrook.edu

^bNuclear Science and Technology Department, Brookhaven National Laboratory, Upton, NY 11973, USA

^cSustainable Energy Technologies Department, Brookhaven National Laboratory, Upton, NY 11973, USA

^dNational Synchrotron Light Source II, Brookhaven National Laboratory, Upton, NY 11973, USA

^eDepartment of Geosciences, Stony Brook University, Stony Brook, NY, 11794, USA

^fCenter for Functional Nanomaterials, Brookhaven National Laboratory, Upton, NY 11973, USA

† Electronic supplementary information (ESI) available. See DOI: 10.1039/d0ta00226g

Upon considering the abundance of transition metals and alkali metals (titanium $\sim 0.1\%$ and sodium $\sim 2\%$), TiS_2 -based systems in Na batteries show high potential for next-generation energy storage.^{9–11} Despite the benefits of the Na– TiS_2 system, using TiS_2 as an intercalation host for the cathode still faces challenges. In particular, the lack of knowledge of TiS_2 structural and chemical evolution in the Na battery hinders the development of this new-type energy storage system.^{6,12–15} Intercalation of Li into TiS_2 layers occurs without changes in the crystalline structure. In contrast, the sodiation process of TiS_2 is more complex. A recent review of the role of Ti in electrode materials for Na-ion batteries summarizes the recent studies for TiS_2 .¹¹ In the cyclic voltammetry of TiS_2 against Na, two plateaus are observed that correspond to two different phase transitions of Na_xTiS_2 ; this feature implies a more sophisticated reaction between Na and TiS_2 .^{16,17} Furthermore, the larger ion radius of Na^+ causes lower diffusivity and higher volume expansion of the host materials during insertion; this results in unfavorable kinetic reactions, potentially leading to some degradation of the performance.¹⁷ As such, gaining a further quantitative understanding of the mechanism in the Na– TiS_2 system is vital to the advancement of the technology and mitigation of the potential prominent issues.

In this work, we investigate the reaction mechanism of Na– TiS_2 , and compare it with the Li– TiS_2 system,^{1,6,18,19} with an emphasis on providing quantitative, multi-modal analysis. To reveal the structural and chemical evolution of Na intercalation into TiS_2 , the *operando* synchrotron-based X-ray absorption spectroscopy (XAS) and *ex situ* X-ray powder diffraction (XPD) measurements were employed. The number of chemical species involved in the reaction was determined by the Multivariate Curve Resolution-Alternating Least Squares (MCR-ALS) method, applied to the *operando* X-ray Absorption Near-Edge Structure (XANES) spectral data.²⁰ A characteristic of the MCR-ALS method is that it determines the number of phases without pre-existing knowledge or assumption, and thus can be complementary to the XPD measurements. The modeling of

operando Extended X-ray Absorption Fine Structure (EXAFS) spectra was used to resolve the local structural changes, quantifying the coordination numbers and interatomic distances of the structure during the electrochemical reactions and phase transformation; such analysis is important for understanding the reaction mechanism and correlating with the battery performance. To identify the intermediate phases during Na intercalation, Rietveld refinement in XPD, as a complementary technique of XAS, was also conducted. By integrating all the information coherently together from combined theory and multi-modal synchrotron studies, this work provides a holistic understanding of the structural and chemical evolution of TiS_2 , as well as contributes to the methodological development.

2. Methods

2.1. Preparation of synchrotron *operando* cells and *ex situ* cells

The assembling of battery cells was conducted in an Ar-filled glovebox located in a humidity-controlled dry laboratory. In this work, an optically transparent tube cell, described previously,²¹ was used for synchrotron *operando* XAS experiments as shown in Fig. 1. The design of the tube cell enables direct observation on both anode and cathode sides, which can then be aligned with the X-ray beam at synchrotron beamlines. In our design, a Kapton (polyimide) tube was used as the cell body, with an inner diameter of 2.06 mm and a wall thickness of 25.4 μm . The current collectors were an aluminum rod for the cathode and a stainless-steel rod for the anode. The TiS_2 cathode slurry was composed of TiS_2 (Sigma Aldrich): carbon black (Super C65, Imerys): polyvinylidene difluoride (PVDF, Alfa Aesar) in a 30 : 15 : 5 ratio by weight. This was mixed in *N*-methyl-2-pyrrolidone (NMP, Sigma Aldrich) and directly coated onto the surface of the aluminum rod with a solid loading of $\sim 1.4 \text{ mg cm}^{-2}$; the anode was a small lithium or sodium cube of $\sim 1 \text{ mm}^3$ in size. During assembly, a separator layer (Celgard 2325) was sandwiched between the cathode and anode to

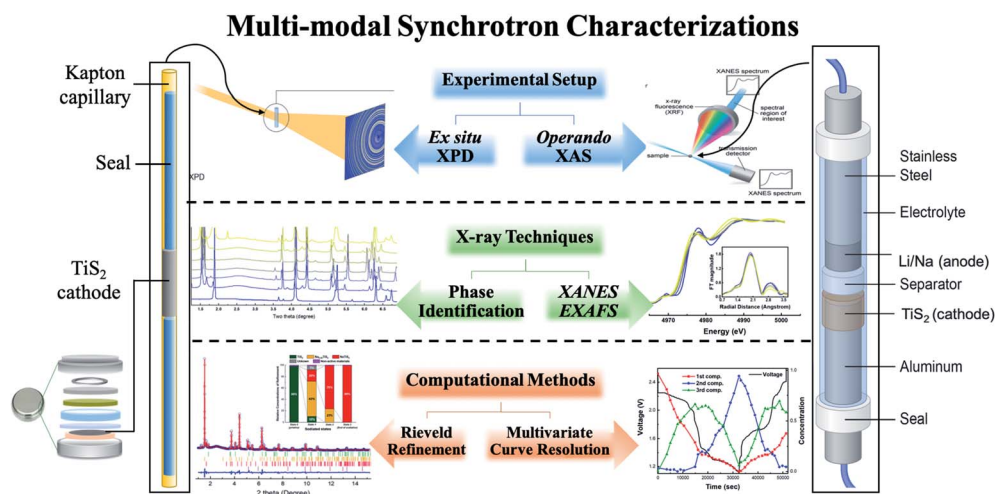


Fig. 1 Schematic of the multi-modal synchrotron characterizations for the *operando* and *ex situ* experiments at various beamlines and the corresponding techniques/analysis applied.

prevent shorting. The cell was then sealed with epoxy adhesive. The electrolyte used for the Li cell was lithium bis(trifluoromethane)sulfonimide (LiTFSI, 1.0 M) dissolved in 1,2-dimethoxyethane (DME) and 1,3-dioxolane (DOL) (1 : 1 by volume ratio). The electrolyte for Na was NaClO₄ (1.0 M). The total electrolyte was estimated to be 20 μL. The electrochemical performance of the *operando* cell was determined using a Biologic VSP-300 potentiostat.

In addition to the *operando* tube cell, coin cell tests were carried out to confirm the consistency of the reaction mechanism as compared to the tube cell,²¹ as well as to prepare the samples cycled to different states for the *ex situ* XPD experiment. The TiS₂ cathode slurry mixed with Super C65, PVDF, and NMP was cast on a copper foil with a solid loading of ~2.8 mg cm⁻² using a doctor blade with a thickness of ~20 μm. CR-2032 type coin cells were then assembled in a glove box, following the sequence of TiS₂ cathode, glass fiber separator, Li/Na metal slice, stainless steel and a spring. The electrolyte compositions were the same as for the *operando* cells with the amount of 60 μL. The assembled coin cells were tested using an Arbin battery instrument. After cycling to various interesting states, the assembled coin cells were opened in a glove box. The materials on the cathode were collected and sealed in Kapton capillaries (inner diameter: 1 mm, wall thickness: 0.05 mm) for the powder XRD experiment. Because of the difference in the geometrical configurations, slow discharge/charge rates (≤C/10) were applied to both the coin cells and the *operando* cells to ensure the consistency of the reaction mechanism.²¹

2.2. Synchrotron characterizations

2.2.1. Hard-X-ray absorption spectroscopy. The *operando* XAS experiment of the Ti K-edge was conducted at the Inner-Shell Spectroscopy beamline (ISS, 8-ID), National Synchrotron Light Source II (NSLS-II) of Brookhaven National Laboratory (BNL). The ISS beamline utilizes a damping wiggler source that provides a high flux (~5 × 10¹³ ph s⁻¹) and has an energy range from 4.9 keV to 36 keV, with a 0.5 mm × 0.5 mm (*h* × *v*) spot size. The Ti K-edge absorption spectra were acquired by tuning a cryogenically cooled double crystal Si(111) monochromator, which enabled the energy fly-scanning mode. *Operando* spectra were recorded from the TiS₂ electrode in the fluorescence mode with a passivated implanted planar silicon (PIPS) detector. Scanning and data acquisition times were ~1 min per spectrum. Multiple cells were measured consecutively as they underwent cycling. Data were collected every 8 minutes on each cell, while the Li- or Na-TiS₂ battery was cycled at C/12 rate, a much slower rate than the data acquisition rate. Three spectra were collected at each time point and averaged to further enhance the data quality. With this measurement strategy, the collected spectra accurately represented the chemical changes with high quality. The absorption spectra of Ti and TiS₂ (Sigma Aldrich) standard samples were collected in both transmission and fluorescence modes.

2.2.2. Tender energy X-ray absorption spectroscopy. In addition to probing Ti, the *operando* XANES experiment for sulfur (S) was conducted at the Tender Energy X-ray

Absorption Spectroscopy (TES, 8-BM) beamline at NSLS-II. TES is optimized for spatially resolved XAS in the tender X-ray energy range, 2–5 keV, ideal for S K-edge analysis. TES employs a silicon (111) monochromator, and delivers a flux of approximately 10¹⁰ photons s⁻¹ focused to an 8 μm × 45 μm (*v* × *h*) spot size by a set of Kirkpatrick–Baez mirrors.^{22,23} Sulfur absorption spectra were recorded in fluorescence mode using a solid-state Ge detector positioned perpendicular to the beam direction. To reduce the attenuation of the X-ray intensity at this energy, samples were contained within a Kapton tube and the sample chamber was helium-purged. The scanning and data acquisition time was ~0.5 min per spectrum, with 20 scans averaged per data point. Data were collected every 15 minutes on each cell. The Na-TiS₂ battery was cycled under a C/10 rate upon considering the data collection and beamline instrument session; this rate was slightly faster than the C/12 rate used at the ISS beamline but the battery displayed an identical electrochemical behavior. The absorption spectra of pure S and TiS₂ (Sigma Aldrich) standard samples were measured in fluorescence mode for energy calibration.

2.2.3. X-ray powder diffraction. The *ex situ* XPD experiment was conducted at the X-ray Powder Diffraction beamline (XPD, 28-ID-2) at NSLS-II.²⁴ To reduce the effects of the preferred orientation, the powders from the coin cells cycled to different states were removed from the current collector and sealed in Kapton capillaries. Each sample was measured at five different rotation angles relative to the X-ray beam. A large-area amorphous-silicon digital X-ray detector, with 2048 × 2048 pixels and pixel size of 200 × 200 μm, was used to collect the diffraction patterns. The sample-to-detector distance was first calibrated by using a Ni standard and was determined to be 1566.37 mm. The X-ray beam size was 0.5 mm × 0.5 mm and the wavelength was 0.1877 Å (X-ray energy was 66.05 keV). At this wavelength, the XPD beamline delivers a high intensity for resolving the weak peaks in the X-ray Diffraction (XRD) patterns so that they can be used in the quantitative analysis. The exposure time of each scan was 30 seconds per 2D image.

2.3. Data analysis

2.3.1. X-ray absorption spectroscopy. The Demeter XAS Data Processing and Analysis software package was used to process the XAS data.²⁵ Normalization and background subtraction of the XAS spectra were conducted in Athena; linear regression was used to fit the pre-edge region and a quadratic polynomial was regressed to fit the post-edge region. The Artemis software²⁵ with FEEF^{26,27} was used to conduct modeling in the EXAFS part of the data. The modeling provides the Ti–S and Ti–Ti coordination numbers and neighboring radial distance.

2.3.2. Multivariate curve resolution-alternating least squares. Multivariate Curve Resolution-Alternating Least Squares (MCR-ALS) is a commonly used method based on extracting meaningful information from the pure components in a mixture system through the decomposition of data matrix *D* into the product of *C* and *S*^T matrices that contain pure profiles of components encoded as rows (usually concentrations) and columns (usually spectra), respectively.^{28,29} The model can be

written as $D = CS^T + E$, in which E accounts for residuals not explained by resolved components. Given D as the input matrix, the task of MCR-ALS is to find C and S matrices that minimize E based on user-defined constraints. In this work, we used the MCR-ALS MATLAB package provided by Jaumot *et al.*³⁰ and imposed non-negativity constraints on XANES spectra and concentrations.²⁰ Equal height normalization of the XANES spectra prior to MCR-ALS decomposition did not yield any noticeable differences. The 500 eV energy window of XAS (4900 to 5400 eV) was chosen as the input for MCR-ALS. The tail of each pure component ($\mu(E)$ at 5400 eV) was used for normalization as post-processing.

2.3.3. XPD and Rietveld refinement. Each XPD pattern was integrated azimuthally and reduced to an intensity *vs.* 2θ (diffraction angle) plot. The peak locations were then compared with the standard references to identify the corresponding phases using the Jade (Materials Data, Inc.) and PDF-4+ 2018 (JCPDS-ICDD) commercial software packages. After phase identification, the Rietveld refinements were conducted using TOPAS-Academic V6. Since all four samples contain multiple components, quantitative analysis was used to get the weight percentage of each phase in each sample. The samples have slightly preferred orientation (PO) so a correction for the preferred orientation based on March's procedure³¹ was applied in the refinement.

3. Results and discussion

3.1. Electrochemical characteristics

The representative discharge–charge curves of the first cycle for *operando* cells working at synchrotron beamlines and conventional coin cells tested in the laboratory are shown in Fig. 2. The discharging cut-off voltage was selected to be 1.8 V for Li/TiS₂ and 1.1 V for Na/TiS₂, while the charging cut-off voltage for both cases was 2.6 V. Since the *operando* cells have a different geometrical configuration from the coin cell, the kinetics and the actual capacity could deviate from the reaction in the coin cell. As shown in Fig. 1, the design of the *operando* cell introduced a longer distance (2–6 mm) from the anode to the cathode, asymmetrical electrodes, and uncertainty of the electrode weight.²¹ These factors allow the reaction to reach

equilibrium in a longer time, and it is more challenging to define the exact states when comparing the *operando* cell and coin cell. As a result, the *x*-axis of the relative capacity in Fig. 2 was not normalized by the theoretical capacity value. Instead, the relative capacity was normalized by the capacity value at the fully reacted state. In this way, the difference of the geometrical configuration between *operando* cell and coin cell could be minimized. The chemical states of the two types of cells can then be compared. Hence, after normalization, the observed electrochemical profiles of Li–TiS₂ and Na–TiS₂ in *operando* cells agree well with the coin cell profiles as well as the previous reports.^{3,16,32}

The smooth electrochemical profiles in the lithiation and de-lithiation processes indicate a single-phase reaction. The space groups before lithiation (TiS₂) and after lithiation (LiTiS₂) are all known as *P3m1*.¹⁷ The discharging/charging reaction of Li–TiS₂ only involves the intercalation/de-intercalation of Li ions inserted into and extracted from the space between the TiS₂ layers, which leads to an increase in the lattice parameters. On the other hand, the multi-plateau electrochemical curves in the sodiation and de-sodiation, as shown in Fig. 2(B), imply a likely crystal space group symmetry change, which involves the formation of undetermined intermediate phases^{12,33} in addition to the fully sodiated product, NaTiS₂, whose stable space group is predicted to be *R3m*.¹⁷ To shed light on the structural and chemical evolution of TiS₂ in these two systems, Li ions and Na ions batteries, their *operando* XAS and *ex situ* XPD characterizations are discussed below.

3.2. Chemical evolution by X-ray absorption spectroscopy at Ti and S K-edges

In order to study the structural and chemical changes during the battery reaction, a series of *operando* XAS experiments of TiS₂ against Li and Na were conducted through two synchrotron X-ray beamlines: the ISS and TES at NSLS-II, BNL. The Ti K-edge (4966 eV) XANES was determined at the ISS beamline, while the S K-edge (2472 eV) XANES was determined at the TES beamline, due to their complementary nature.

Fig. 3 shows the *operando* XANES spectra measured at the TiS₂ electrode as a function of different depths of discharge. For both lithiation and sodiation processes in TiS₂, the Ti K-edge

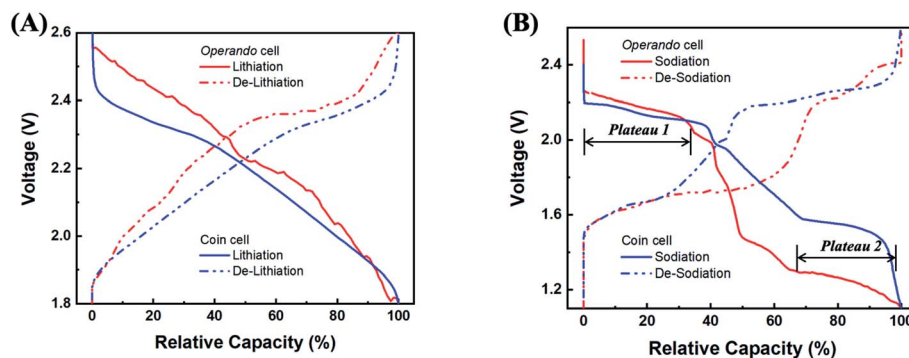


Fig. 2 The electrochemical profiles of the *operando* cell (red lines) as compared with the coin cell (blue lines) for lithiation/de-lithiation in (A) and sodiation/de-sodiation in (B).

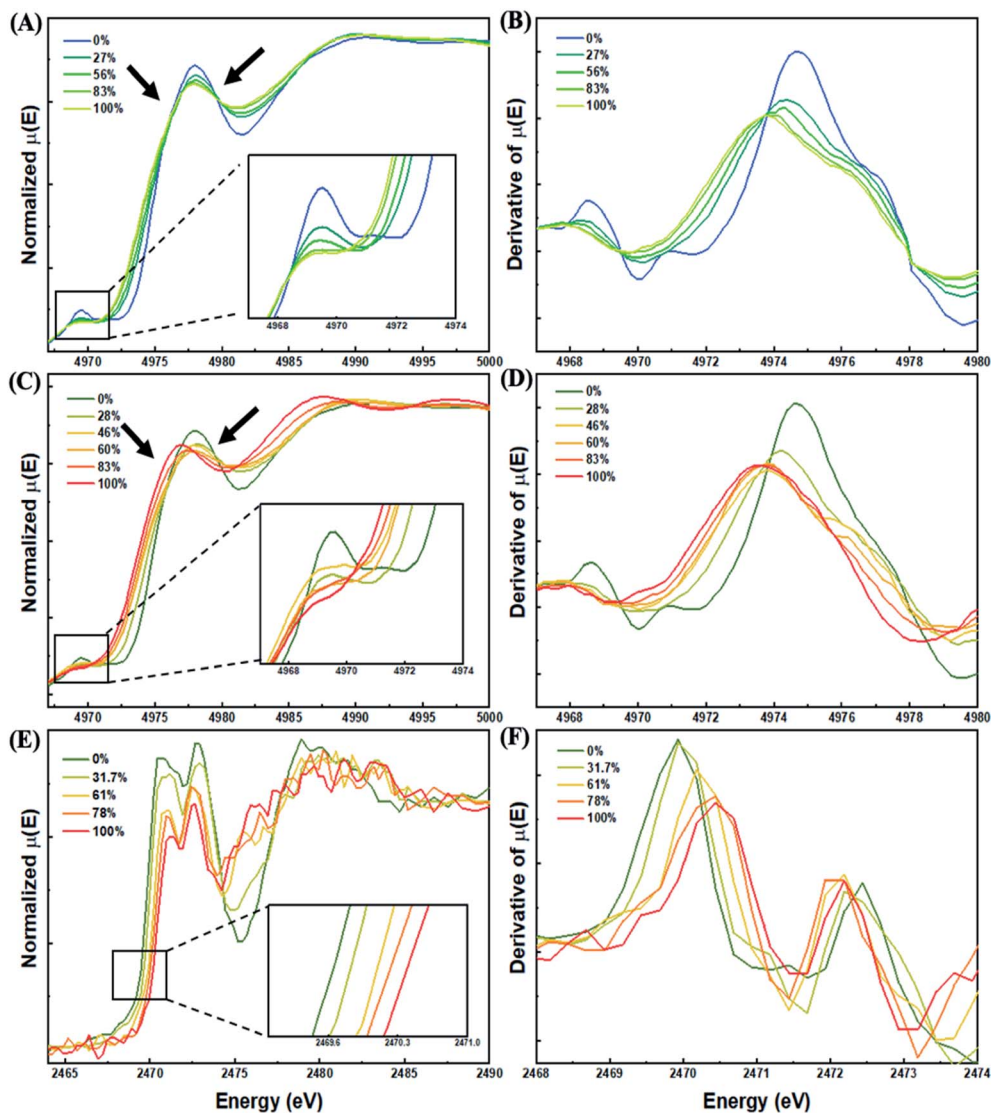


Fig. 3 The *operando* XANES spectra in the first cycle and the corresponding first derivatives. (A and B) The Ti K-edge for the lithiation process; (C and D) the Ti K-edge for the sodiation process; (E and F) the S K-edge for the sodiation process with X-ray attenuation relative to the incident X-ray energy. Insets show the details of the pre-edge features.

positions shifted towards lower energy as shown in Fig. 3(B) and (D) by observing the main peaks moving to lower energy in the first derivative of the X-ray attenuation relative to the incident X-ray energy. The shifts toward lower energy imply that Ti ions of TiS_2 were reduced during discharge, where Ti acted as an electron acceptor during the insertion of alkali ions. Meanwhile, the pre-edge peaks whose details are shown in the insets of Fig. 3(A) and (C) became less prominent as Li or Na was intercalated into TiS_2 layers. These pre-edge peaks are attributed to transitions from the Ti-1s orbital to the Ti-3d/S-3p hybrid orbital in a partially distorted octahedral structure.^{19,34,35} Previous studies have indicated that the decreasing intensity at the pre-edge of Ti in lithiation could be related to the repulsive interaction of inserted Li-ions and Ti-ions in TiS_2 .^{19,35} The insertion may symmetrize the distorted octahedral environment of the Ti atoms to suppress the pre-edge peak,^{19,35} while expanding the

lattice spacing. We observed similar Ti pre-edge suppression during sodiation.

Besides shifts in the main edge and the decrease in the pre-edge peak intensity, the main edge of the XANES spectra in sodiation evolved distinctively once the sodiation reaction exceeded 60% of the capacity, as labeled with an arrow in Fig. 3(C). The spectra exceeding 60% of capacity did not cross each other and led to the elimination of the isosbestic point. Such a clear spectral shape change did not occur in the lithiation case, as shown in Fig. 3(A), where the symmetry group of TiS_2 and Li_xTiS_2 remained unchanged during discharge. The appearance of an isosbestic point in a spectral series is evidence for a simple A-to-B transformation. It could be a chemical state change or phase transformation as long as only two states are involved. These new XANES spectral features in the sodiation of TiS_2 thus indicate that instead of a simple A-to-B transformation, there is an intermediate involved in the sodiation

process.³³ Further quantification analysis needs to be carried out to predict the unknown reaction products of sodiation that correspond to the multi-plateau electrochemical profile as observed in the sodiation of TiS_2 .

The *operando* XANES spectra of the S K-edges and their first derivatives during sodiation are shown in Fig. 3(E) and (F). From the spectra, the edge positions of S shift to higher energy during sodiation. This result is consistent with the analysis of the density of states done by Zhang *et al.*¹⁹ In their report, the electrons transferred from Li ions not only to titanium but also to sulfur during intercalation, and there was also a conversion reaction. This may imply that sulfur is also involved in the sodiation reaction and receives electrons. The slightly noisy data observed in the TES S-edge XANES may be attributed to the challenge of obtaining data in *operando* cells with a high signal-to-noise ratio in the tender X-ray range; however, it is sufficient to provide information regarding the battery reaction evolution.

Although the change in the oxidation state and geometrical symmetry in the lithiation and sodiation reactions could be extracted from the *operando* XANES spectra, identifying the number and the nature of the chemical components involved in the sodiation process required further analysis. MCR-ALS method,³⁶ was applied to the *operando* XANES data sets to unravel pure spectral components. In the MCR-ALS method, the number of pure components is a user-defined variable. Evolving Factor Analysis (EFA)^{37,38} is a commonly used method to estimate the number of pure components. Fig. S1(A and B)† shows the EFA calculation for lithiation and sodiation XANES spectra. Although the first two factors are emergent, higher-order factors

are not easily distinguishable from the noise level. Therefore, we varied and tested the number of pure components between 2 and 8. The χ^2 values of the Pearson correlation coefficient (goodness of fit) versus the number of pure components in deconvolution are also shown in Fig. S1(C);† note that this goodness of fit value does not improve significantly after 3 components. The calculated spectra of pure components for both lithiation and sodiation processes using 2–4 components are shown in Fig. S1(D–I).† In both lithiation and sodiation, the deviation of the calculated spectra from the experimental spectra decreased as the number of components increased; this trend is statistically expected when calculating the goodness of fit. For lithiation, it is well understood that the intercalation of Li in TiS_2 does not cause any phase transformation; *i.e.*, TiS_2 and LiTiS_2 share the same space group and only the expansion of lattice parameters occurs.^{3,18} Therefore, the lithiation process is known to be a single-phase and two-component reaction. This is consistent with the present MCR-ALS analysis. The third component from the deconvolution resembles the second component, suggesting that two pure components are sufficient to describe the phase transformation. In comparison, the presence of a third component with distinct XANES features is evident in the MCR-ALS results for sodiation. The two-component solution for the lithiation spectra reproduced experimentally known phases. On the other hand, the second and third components were almost identical to the three-component case, as shown in Fig. S1(E).† In the case of sodiation, the goodness of fit significantly improved upon the inclusion of the third component. However, the inclusion of the

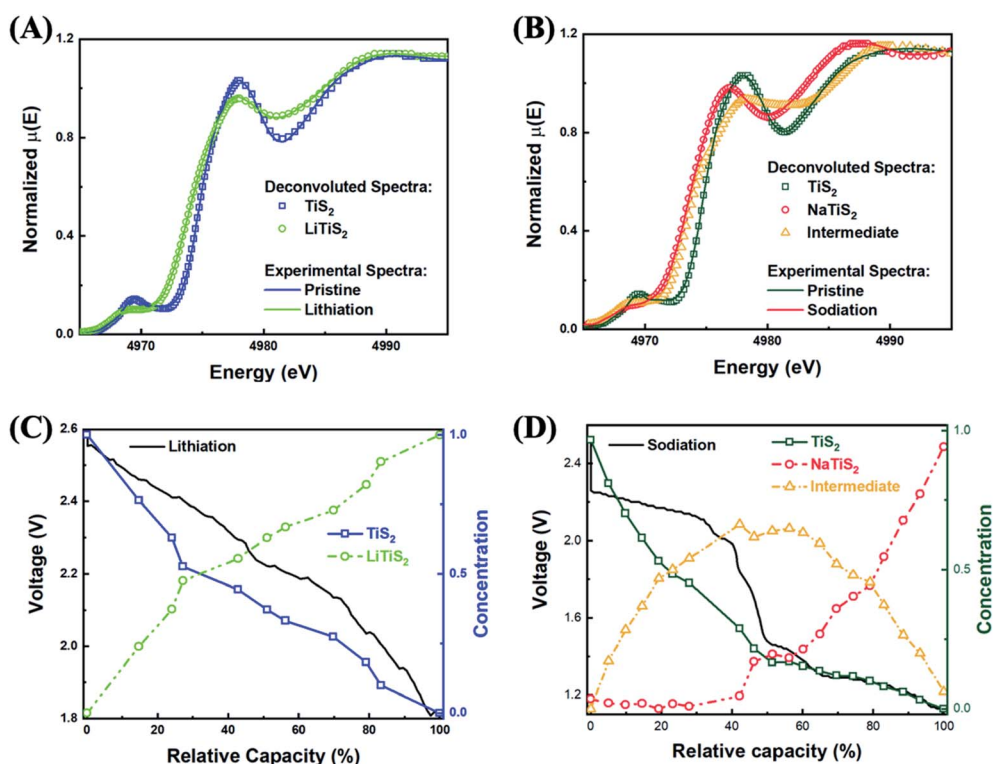


Fig. 4 MCR-ALS analysis of the *operando* XANES series: deconvoluted pure components for lithiation (A) and sodiation (B); the concentration evolution of two-component and three-component reactions for lithiation (C) and sodiation (D), respectively.

fourth component produced unrealistic XANES spectra as shown in the revised Fig. S1(F and I).† The final deconvoluted pure-component spectra for the lithiation and sodiation processes are shown in Fig. 4(A) and (B), with two and three components, respectively.

The concentration evolution of the two-component reaction for lithiation is shown in Fig. 4(C) and the three-component sodiation reaction in Fig. 4(D). As seen in Fig. 4(C), the lithiation process starts with the 1st component, whose concentration gradually reduces, while the end-product corresponding to the 2nd component gradually increases in concentration till the end of the lithiation. The starting phase (*i.e.* the 1st component) from spectral deconvolution is thus identified as

the pristine phase TiS_2 , whereas the 2nd component is identified as the lithiated Li_xTiS_2 phase.

In comparison, the sodiation process is shown in Fig. 4(D). Similar to the lithiation process, the decrease in the 1st component from the start of the sodiation and the appearance of the 2nd component during the sodiation were observed, where the 1st component was identified as TiS_2 and the 2nd component as the fully sodiated NaTiS_2 . Interestingly, an additional phase, the 3rd component, appeared during the sodiation reaction and reached its maximum at the capacity of about 50%. Furthermore, the main edge positions from the 1st component (pristine TiS_2) to the 3rd component (additional phase), and finally to the 2nd component (the end product of sodiation), displayed a shift toward lower energy; this shift is

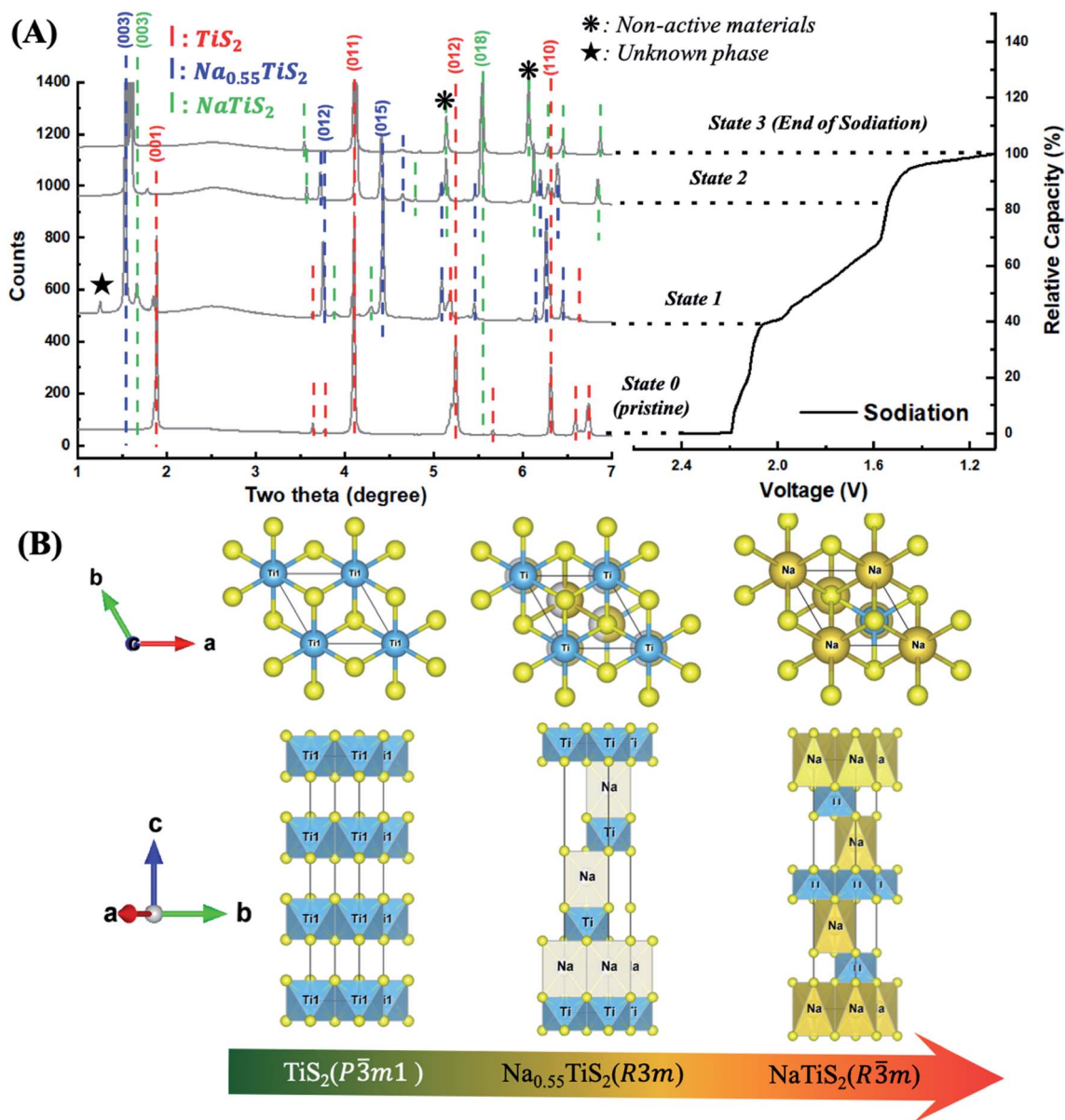


Fig. 5 (A) The *ex situ* XPD patterns from the TiS_2 electrode aligned with its corresponding electrochemical profile during sodiation. The peaks from non-active materials including the current collector are marked with (*). (B) The major crystal structures involved in sodiation at each cycled state.³⁹

consistent with the experimental spectra as shown previously in Fig. 3(D). These results indicate that the 3rd component is an intermediate product that was introduced during sodiation but diminished at the end of sodiation.

3.3. Phase identification and refinement by X-ray powder diffraction

To determine the intermediate phase of sodiation, shown as the 3rd component in the MCR-ALS analysis of XANES in the previous section, we conducted XPD measurements on samples in different states of charge and carried out Rietveld refinement on these XPD patterns. The electrochemical data for the *ex situ* XPD samples are included in Fig. S4,† with each state labeled. The chemical species with different long-range orders are identified at various discharging depth in Fig. 5(A), while their corresponding relative concentrations are calculated from refinements and are summarized in Fig. 6.

The refinement profiles in Fig. S2† and the fitting parameters in Table S1† confirm that three phases, TiS₂, Na_{0.55}TiS₂, and NaTiS₂, are involved in the sodiation reaction.^{31,40} As the pristine TiS₂ is sodiated to *State 1*, the system evolves into a three-component mixture where Na_{0.55}TiS₂ is the main component. As the sodiation process moves to *State 2*, TiS₂ is fully transformed into Na_{0.55}TiS₂ and NaTiS₂, with NaTiS₂ becoming dominant. Finally, the system turns into a pure phase of NaTiS₂ at the end of the sodiation.

The intensity variation of the diffraction peaks, *e.g.*, TiS₂ (001) peak, as well as Na_{0.55}TiS₂ (003) and NaTiS₂ (003), is shown in Fig. 5(A). At *State 1*, the strongest peak is Na_{0.55}TiS₂ (003), which has the largest *c*-axis lattice parameter. However, the *c*-axis length becomes shorter as the diffraction peaks shift to higher diffraction angles during further sodiation. This is because the space group of Na_{0.55}TiS₂ is *R3m*, while the space group of NaTiS₂ is *R3̄m*.

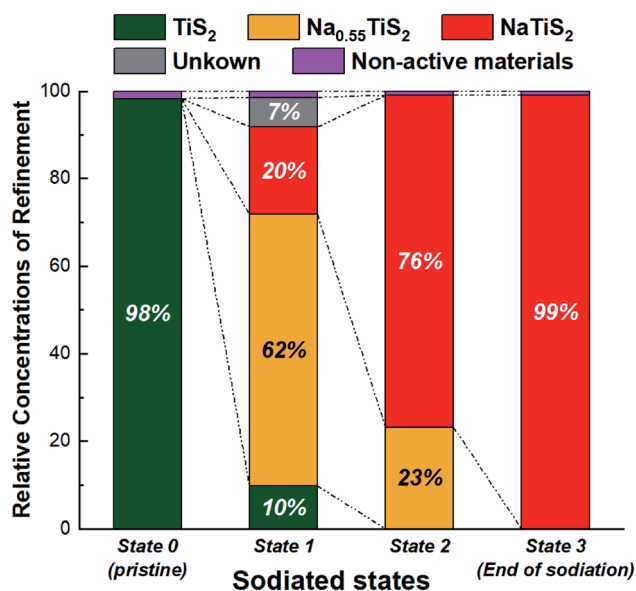


Fig. 6 The relative concentrations (%) calculated by Rietveld refinement at different discharging states as labeled in Fig. 5(A); the unknown phase is assumed to be Na_{0.3}TiS₂ in the quantitative phase analysis.

When a Na atom is inserted into the TiS₂ layers, it will stack on top of a Ti atom to form Na_{0.55}TiS₂ first. As more Na ions are driven into TiS₂, an offset along the *a*-*b* plane occurs so that the stacked Na atoms are no longer directly on top of Ti atoms; the system prefers this offset to reduce the lattice expansion and to stabilize the crystal structure. This offset makes the *c*-axis parameter of NaTiS₂ smaller than Na_{0.55}TiS₂, as illustrated in Fig. 5(B). The presence of three phases during the sodiation of TiS₂ is consistent with the calculated phase diagram of Na_{*x*}TiS₂ that shows the O1, P3 and O3 stacking of TiS₂ layers;⁴¹ nevertheless, there is still an unknown phase at *State 1*. A *P3m1* structure, NaTi₃S₆, with *c* = 25.83 Å, which is isostructural to the lithium counterpart, may be adopted to fit the peaks of this “unknown phase”; note that NaTi₃S₆ is not a measured structure in the database where lattice parameters are confirmed by experiment. The structure and lattice parameters of NaTi₃S₆ were calculated and are believed to be a metastable phase in the sodiation of TiS₂. Overall, this unknown phase contributes ~7% to all the crystalline phases detected. Since the model accounts for only 3 weak peaks in the XPD patterns and is not a known structure in existing structure databases, we cannot confirm its structure with our XPD data. Some reports indicated the observation of certain intermediate phases, Na_{0.22}TiS₂ (ref. 12 and 14) and Na_{0.25}TiS₂,¹⁵ but the lattice parameters are inconsistent with the XPD results shown here. Recently, Wang *et al.* reported the investigation of the sodiation process in TiS₂ nanoflakes by *in situ* transmission electron microscopy.⁴² They predicted the formation of the Na_{0.33}TiS₂ phase and confirmed it as a thermodynamically preferred phase by first-principles calculations, which is consistent with our hypothesis of the unknown phase in Fig. 5(A). Overall, this unknown phase could be a metastable Na_{*x*}TiS₂ phase with *x* < 1/3.

The ESI† includes a summary of the quantification results of MCR-ALS and Rietveld refinements based on relative capacity (Table S2†) and absolute capacity (Table S3†). These two analyses show agreement regarding the general trend and yet differ in the quantitative details as discussed in the ESI.† These discrepancies represent the conditions in multi-modal characterization, as well as comparing the *operando* and *ex situ* studies. XRD detects long-range ordered crystalline structures while XAS not only measures ordered phases but is also sensitive to non-crystalline and highly disordered materials. *Operando* studies generally require modification of the battery cells and measurement is performed when materials are under non-equilibrium states during reactions. In contrast, the samples measured under *ex situ* or post-cycled analysis can be generally measured under ideal technical conditions and yet, not while the reactions are taking place. While comparing the results quantitatively depends on the experimental conditions, the results show that both *operando* and *ex situ* across multiple characterization techniques can be used together to provide complementary information for a more complete analysis.

3.4. Atomic structure modeling using extended X-ray absorption fine structure (EXAFS)

The above discussions show a quantitative analysis of the chemical and structural revolutions of TiS₂ in lithiation and

sodiation based on the *operando* XANES and *ex situ* XPD studies. To further understand the local chemical and structural changes, we created an atomic model to fit the EXAFS region in the Ti XAS data. The key fitting parameters include the coordination number and interatomic distance for Ti-S (first shell) and Ti-Ti (second shell) of TiS_2 . Fig. 7(A) and (B) show the radial distribution function of the EXAFS spectra in *operando* XAS experiments during lithiation and sodiation at various reaction depths, obtained by calculating the Fourier Transform (FT) of the EXAFS spectra. The corresponding k^2 -weighted EXAFS $\chi(k)$ spectra and the FT window are shown in Fig. S6.†

The intensities of the second-shell (Ti-Ti) in the radial distribution functions decreased in both lithiation and sodiation reactions. This observation is consistent with the EXAFS fitting results shown in Fig. 7(C) and (D). During lithiation, the number of S atoms surrounding the Ti core atom showed little change from 6 to 5.77 while the coordination number of Ti-Ti

(second shell) decreased from 6 to 4.67. Similarly, during sodiation, the number of neighboring S atoms around Ti only changed from 6 to 5.69, whereas the coordination number of Ti-Ti reduced from 6 to 4.26. This implies that the insertion of Li or Na ions resulted in a local structural change in TiS_2 on the Ti-Ti shell, which may cause the formation of sub-layer TiS_2 with fewer neighboring Ti around Ti core atoms, making the layers discontinuous.

The distributions of bond length in Ti-S and Ti-Ti shells for lithiation and sodiation are displayed in Fig. 7(E) and (F), respectively. The bonding lengths of both the first shell (Ti-S) and second shell (Ti-Ti) were elongated during both lithiation and sodiation reactions. The increasing interatomic distance of Ti-S and Ti-Ti indicates that the two reactions not only open the space between TiS_2 layers but also increase the space on the *a-b* plane perpendicular to the *c*-axis direction. Compared to the crystal structure derived from XPD, the results of expansion on

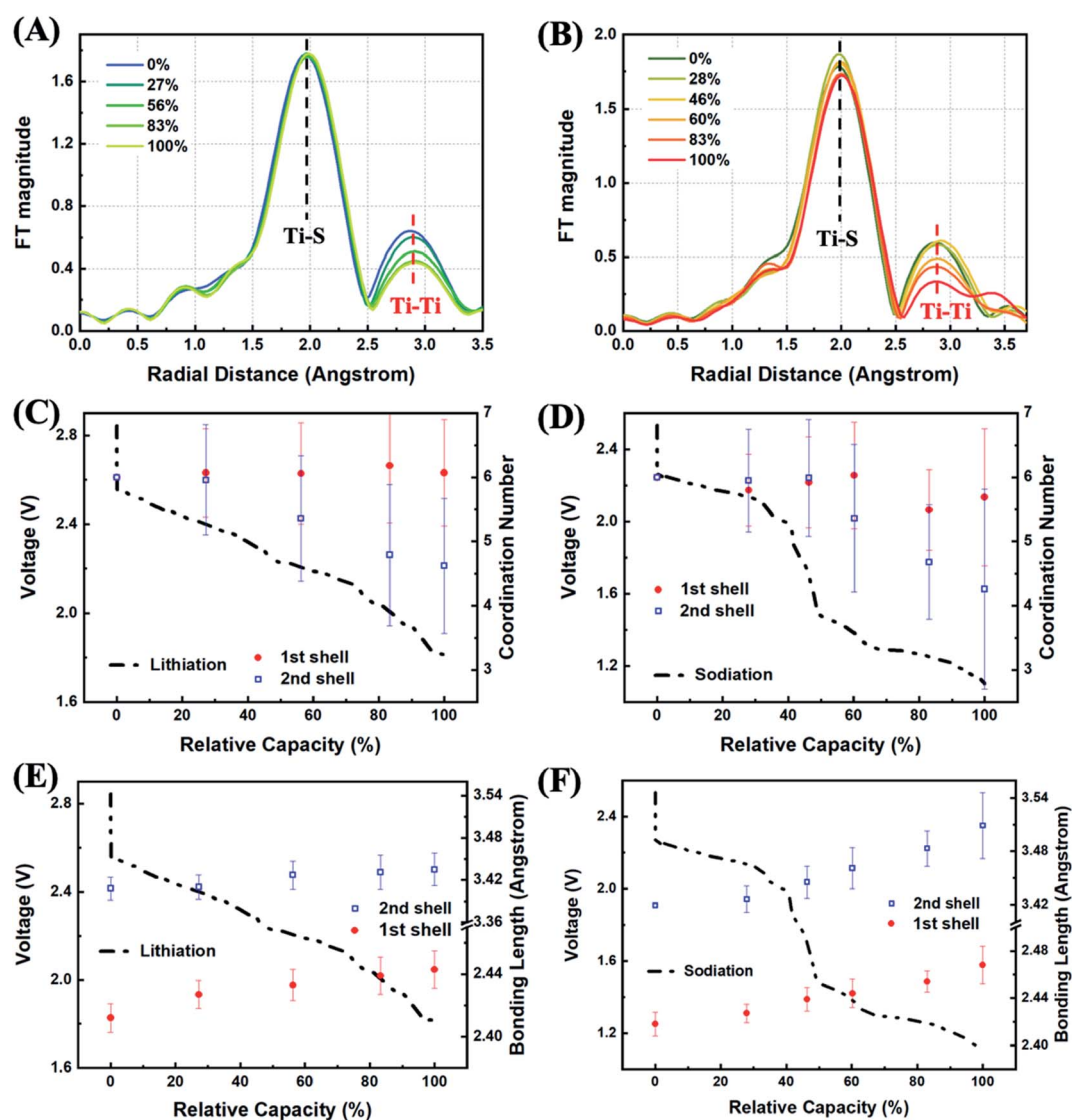


Fig. 7 The radial distribution functions of the EXAFS part in *operando* XAS experiments during (A) lithiation and (B) sodiation at the various discharging states. The modeling results of EXAFS spectra on Ti-S (1st shell) and Ti-Ti (2nd shell): (C and D) Coordination number and (E and F) bonding length evolutions in both lithiation and sodiation.

Table 1 The refined structural parameters for TiS_2 electrodes obtained from *operando* XAS data at the end states of the battery reaction; the parameters of the a -axis equal to the Ti–Ti bond derived from XPD are included for comparison

Parameters		Pristine TiS_2	Full lithiation	Full de-lithiation	Full sodiation	Full de-sodiation
Coordination number	Ti–S	6	6.07 ± 0.83	6.14 ± 0.78	5.69 ± 1.07	5.70 ± 0.68
	Ti–Ti	6	4.62 ± 1.05	5.26 ± 0.92	4.26 ± 1.56	5.98 ± 1.00
Bond length (Å)	Ti–S	2.430	2.44 ± 0.01	2.42 ± 0.01	2.47 ± 0.02	2.44 ± 0.01
	Ti–Ti	3.410	3.44 ± 0.02	3.41 ± 0.02	3.51 ± 0.04	3.44 ± 0.02
a -axis from XPD (Å)		3.41	3.42	3.55		

the a – b plane from EXAFS in lithiation and sodiation are quantitatively consistent with the lattice parameters calculated from XPD results, as shown in Table 1.

In addition, several works reported a decay in the coulombic efficiency after the first cycle of the Li– TiS_2 ^{6,19} and Na– TiS_2 .^{12,33} In Fig. S5,† electrochemical cycling tests of Li– TiS_2 and Na– TiS_2 coin cells reacted at 0.1C rate are provided. This decay is usually attributed to the formation of the solid electrolyte interphase (SEI) in the lithiation case.^{6,19} The formation of the SEI would permanently consume part of the active materials and thus lead to the fading of the specific capacity in batteries. As a result, the reversibility of the active materials after the first cycle is another important issue for the application of Li/Na– TiS_2 batteries. Thus, the modeling of the EXAFS spectra during de-lithiation and de-sodiation was carried out as shown in Fig. S3.† For both processes, the Ti–Ti coordination number and bonding length of the 1st & 2nd shells were found to be close to those of the TiS_2 state. However, the de-lithiation and de-sodiation did not recover the pure TiS_2 phase. As summarized in Table 1, in the case of the Li– TiS_2 battery, the bond lengths recovered within 0.01 Å, whereas the Ti–Ti coordination number changed from 6 to 5.26. In contrast, in the case of the Na– TiS_2 battery, the Ti–Ti coordination number was fully restored but the Ti–Ti bond length increased, indicating a larger lattice expansion. The incomplete reactions in both de-lithiation and de-sodiation agree with the decay in the coulombic efficiency after the first cycle, but the mechanism behind this decay differs between Li and Na.

4. Conclusion

This work provides further mechanistic insights into alkali metal insertion into layered transition metal dichalcogenides during battery charge and discharge. By applying a combination of *operando* XAS, MCR-ALS, and *ex situ* XPD, we investigated the chemical and structural evolutions of TiS_2 during sodiation in order to understand the reaction mechanism of TiS_2 in Na-ion batteries. From the XANES spectra, the edge shifting toward lower energy indicated that Ti ions were reduced in both the lithiation and sodiation reactions. Simultaneously, sulfur also participated in the redox reaction in sodiation.

The XANES spectral shape variations, *e.g.*, isosbestic points, imply that the lithiation is a pure intercalation reaction, whereas sodiation involves a more complex structural change. *Via* MCR-ALS analysis, the calculations identified chemical components that participate in lithiation and sodiation. The deconvoluted spectra showed that the lithiation and sodiation processes are

two- and three-component reactions respectively. The third component in the sodiation is an intermediate phase.

The three components involved in the Na– TiS_2 reaction were found to be a conversion process from TiS_2 to $\text{Na}_{0.55}\text{TiS}_2$, and finally to NaTiS_2 using XPD experiments and Rietveld refinements. During sodiation, the c -axis length started to increase when TiS_2 ($3c = 17.1$ Å) was transformed into $\text{Na}_{0.55}\text{TiS}_2$ ($c = 20.94$ Å) but then decreased when $\text{Na}_{0.55}\text{TiS}_2$ became NaTiS_2 ($c = 20.58$ Å). The c parameter in TiS_2 was tripled since it has only one MO_6 octahedral layer in its unit cell, whereas the Na_xTiS_2 phases have three. Overall, the crystal structure changed from $\text{Na}_{0.55}\text{TiS}_2$ ($R3m$) to NaTiS_2 ($R3m$) and led to an a – b plane offset to ‘unstack’ the Na atoms from the Ti atoms and shrinkage of the c -axis, thereby stabilizing the structure. The main reason for the different intercalation mechanisms is believed to be the larger size of the Na ion as compared to the Li-ion.

From the EXAFS modeling, the structural evolution in lithiation/de-lithiation and sodiation/de-sodiation had different impacts on the decay of the coulombic efficiency after cycling. The increasing interatomic distances of Ti–S and Ti–Ti shells in both lithiation and sodiation reactions show that the intercalation of Li and Na atoms not only leads to c -axis expansion but also to a lattice space opening along the a – b plane. The decreasing coordination numbers of the Ti–Ti shell may indicate the local structural change to form TiS_2 sub-layers. However, the incomplete recovery of the Ti–Ti coordination number in de-lithiation implies some degree of breakdown of the structure; this results in a known degree of decay of Coulombic efficiency.^{6,12} In contrast, sodiation involves structural changes including shifts in the stacking of layers; this rearrangement leads to the incomplete recovery of the c lattice parameter but better recovery of the Ti–Ti coordination number. This mechanism may explain why Na– TiS_2 has a better restoration of active materials, by re-structuring after every cycle, and potentially better lifetime efficiency than Li. The different structural recoveries among de-lithiation and de-sodiation may explain why Li– TiS_2 and Na– TiS_2 have different cycling performances; however, further work is required to understand this structure–performance correlation. Analysis of the structural changes in multiple cycles for both crystalline and amorphous phases, by combining EXAFS, diffraction and other techniques, would be invaluable. The studies to fully understand the mechanism of TiS_2 would enhance the design of the optimal TiS_2 matrix for Li and Na for various purposes, *e.g.*, Li– TiS_2 for fast rate and small-scale application and Na– TiS_2 for slow rate but large-scale energy storage.

Author contributions

K. Sun, H. Gan, and Y.-cK Chen-Wiegart developed the initial research concept, with further discussion on multimodal data analysis with E. Stavitski and D. Lu. Y.-cK Chen-Wiegart wrote the synchrotron beamtime proposals with the input from H. Gan and K. Sun to obtain instrument time. K. Sun designed the *operando* cells. C.-H. Lin assembled the cells and performed the electrochemical measurements. E. Stavitski designed, commissioned and setup ISS beamline. P. Northrup designed, commissioned and setup TES beamline. C.-H. Lin, C. Zhao, and Y.-cK Chen-Wiegart conducted the synchrotron XAS experiments with E. Stavitski at ISS and with P. Northrup at TES. C.-H. Lin performed the XAS data analysis under the supervision of E. Stavitski and Y.-cK Chen-Wiegart. M. Topsakal and D. Lu conducted the MCR-ALS analysis. C.-H. Lin and C. Zhao disassembled the *ex situ* cells and prepared powder samples for XPD experiments. C.-H. Lin, C. Zhao and Y.-cK Chen-Wiegart conducted the synchrotron XPD experiments with J. Bai and E. Dooryhee. C.-H. Lin analyzed the XPD data under the guidance of J. Bai. J. Bai conducted the Rietveld refinement. C.-H. Lin, M. Topsakal, K. Sun, J. Bai, H. Gan, D. Lu, E. Stavitski and Y.-cK Chen-Wiegart interpreted the data. C.-H. Lin wrote the manuscript under the supervision of Y.-cK Chen-Wiegart, with the inputs from all co-authors.

Conflicts of interest

There are no conflicts to declare.

Acknowledgements

This work is supported by the U.S. Department of Energy (DOE) Office of Energy Efficiency and Renewable Energy under the Advanced Battery Materials Research (BMR) program, Contract No. DE-SC0012704. This research used resources 8-ID (ISS), 8-BM (TES) and 28-ID-2 (XPD) beamlines of the National Synchrotron Light Source II, a U.S. DOE Office of Science User Facility operated for the DOE Office of Science by Brookhaven National Laboratory under Contract No. DE-SC0012704. We acknowledge Dr Klaus Attenkofer for his support during ISS beamtime. K. Chen-Wiegart and C.-H. Lin acknowledge the support by the Department of Materials Science and Chemical Engineering, the College of Engineering and Applied Sciences, and the Stony Brook University. This research used resources of the Center for Functional Nanomaterials, which is a U.S. DOE Office of Science Facility, and the Scientific Data and Computing Center, a component of the Computational Science Initiative, at Brookhaven National Laboratory under Contract No. DE-SC0012704.

References

- 1 E. A. Suslov, O. V. Bushkova, E. A. Sherstobitova, O. G. Reznitskikh and A. N. Titov, *Ionics*, 2016, **22**, 503–514.
- 2 G. B. Haxel, J. B. Hedrick and G. J. Orris, *U.S. Geological Survey*, 2002, USGS Fact Sheet 087-002.
- 3 M. S. Whittingham, *Science*, 1976, **192**, 1126–1127.
- 4 A. H. Thompson, *Phys. Rev. Lett.*, 1975, **35**, 1786–1789.
- 5 S. N. Li, J. B. Liu and B. X. Liu, *J. Power Sources*, 2016, **320**, 322–331.
- 6 A. Chaturvedi, P. Hu, V. Aravindan, C. Kloc and S. Madhavi, *J. Mater. Chem. A*, 2017, **5**, 9177–9181.
- 7 B. B. Tian, W. Tang, K. Leng, Z. X. Chen, S. J. R. Tan, C. X. Peng, G. H. Ning, W. Fu, C. L. Su, G. Y. W. Zheng and K. P. Loh, *ACS Energy Lett.*, 2017, **2**, 1835–1840.
- 8 K. Sun, Q. Zhang, D. C. Bock, X. Tong, D. Su, A. C. Marschilok, K. J. Takeuchi, E. S. Takeuchi and H. Gan, *J. Electrochem. Soc.*, 2017, **164**, A1291–A1297.
- 9 M. D. Slater, D. Kim, E. Lee and C. S. Johnson, *Adv. Funct. Mater.*, 2013, **23**, 947–958.
- 10 N. Yabuuchi, K. Kubota, M. Dahbi and S. Komaba, *Chem. Rev.*, 2014, **114**, 11636–11682.
- 11 Y. S. Wang, W. Zhu, A. G. Fi, C. Kim and K. Zaghbi, *Frontiers in Energy Research*, 2019, **7**, 12.
- 12 Y. P. Liu, H. T. Wang, L. Cheng, N. Han, F. P. Zhao, P. R. Li, C. H. Jin and Y. G. Li, *Nano Energy*, 2016, **20**, 168–175.
- 13 A. Chaturvedi, E. Edison, N. Arun, P. Hu, C. Kloc, V. Aravindan and S. Madhavi, *ChemistrySelect*, 2018, **3**, 524–528.
- 14 H. W. Tao, M. Zhou, R. X. Wang, K. L. Wang, S. J. Cheng and K. Jiang, *Adv. Sci.*, 2018, **5**, 7.
- 15 B. Han, S. L. Chen, J. Zou, R. W. Shao, Z. P. Dou, C. Yang, X. M. Ma, J. Lu, K. H. Liu, D. P. Yu, L. P. Wang, H. C. Wang and P. Gao, *Nanoscale*, 2019, **11**, 7474–7480.
- 16 G. H. Newman and L. P. Klemann, *J. Electrochem. Soc.*, 1980, **127**, 2097–2099.
- 17 S. P. Ong, V. L. Chevrier, G. Hautier, A. Jain, C. Moore, S. Kim, X. H. Ma and G. Ceder, *Energy Environ. Sci.*, 2011, **4**, 3680–3688.
- 18 Q. Zhang, D. C. Bock, K. J. Takeuchi, A. C. Marschilok and E. S. Takeuchi, *J. Electrochem. Soc.*, 2017, **164**, A897–A901.
- 19 L. Zhang, D. Sun, J. Kang, H. T. Wang, S. H. Hsieh, W. F. Pong, H. A. Bechtel, J. Feng, L. W. Wang, E. J. Cairns and J. H. Guo, *Nano Lett.*, 2018, **18**, 4506–4515.
- 20 P. Conti, S. Zamponi, M. Giorgetti, M. Berrettoni and W. H. Smyrl, *Anal. Chem.*, 2010, **82**, 3629–3635.
- 21 K. Sun, C. H. Zhao, C. H. Lin, E. Stavitski, G. J. Williams, J. M. Bai, E. Dooryhee, K. Attenkofer, J. Thieme, Y. C. K. Chen-Wiegart and H. Gan, *Sci. Rep.*, 2017, **7**, 10.
- 22 P. Northrup, A. Leri and R. Tappero, *Protein Pept. Lett.*, 2016, **23**, 300–308.
- 23 P. Northrup, *J. Synchrotron Radiat.*, 2019, **26**, 2064–2074.
- 24 X. B. Shi, S. Ghose and E. Dooryhee, *J. Synchrotron Radiat.*, 2013, **20**, 234–242.
- 25 B. Ravel and M. Newville, *J. Synchrotron Radiat.*, 2005, **12**, 537–541.
- 26 J. J. Rehr and R. C. Albers, *Rev. Mod. Phys.*, 2000, **72**, 621–654.
- 27 J. J. Rehr, J. J. Kas, M. P. Prange, A. P. Sorini, Y. Takimoto and F. Vila, *C. R. Phys.*, 2009, **10**, 548–559.
- 28 R. Tauler, *Chemom. Intell. Lab. Syst.*, 1995, **30**, 133–146.
- 29 R. Tauler, A. Smilde and B. Kowalski, *J. Chemom.*, 1995, **9**, 31–58.

- 30 J. Jaumot, A. de Juan and R. Tauler, *Chemom. Intell. Lab. Syst.*, 2015, **140**, 1–12.
- 31 A. March, *Z. Kristallogr.*, 1932, **81**, 285–297.
- 32 E. J. Frazer and S. Phang, *J. Power Sources*, 1981, **6**, 307–317.
- 33 H. S. Ryu, J. S. Kim, J. S. Park, J. W. Park, K. W. Kim, J. H. Ahn, T. H. Nam, G. X. Wang and H. J. Ahn, *J. Electrochem. Soc.*, 2013, **160**, A338–A343.
- 34 F. Farges, G. E. Brown and J. J. Rehr, *Geochim. Cosmochim. Acta*, 1996, **60**, 3023–3038.
- 35 D. Zhou, S. Permien, J. Rana, M. Krengel, F. Sun, G. Schumacher, W. Bensch and J. Banhart, *J. Power Sources*, 2017, **342**, 56–63.
- 36 W. Zhang, M. Topsakal, C. Cama, C. J. Pelliccione, H. Zhao, S. Ehrlich, L. J. Wu, Y. M. Zhu, A. I. Frenkel, K. J. Takeuchi, E. S. Takeuchi, A. C. Marschilok, D. Y. Lu and F. Wang, *J. Am. Chem. Soc.*, 2017, **139**, 16591–16603.
- 37 M. Maeder, *Anal. Chem.*, 1987, **59**, 527–530.
- 38 H. R. Keller and D. L. Massart, *Chemom. Intell. Lab. Syst.*, 1992, **12**, 209–224.
- 39 K. Momma and F. Izumi, *J. Appl. Crystallogr.*, 2011, **44**, 1272–1276.
- 40 K. Cenzual, L. M. Gelato, M. Penzo and E. Parthe, *Acta Crystallogr., Sect. B: Struct. Sci., Cryst. Eng. Mater.*, 1991, **47**, 433–439.
- 41 M. D. Radin and A. Van der Ven, *Chem. Mater.*, 2016, **28**, 7898–7904.
- 42 X. Z. Wang, Z. P. Yao, S. Hwang, Y. Pan, H. Dong, M. S. Fu, N. Li, K. Sun, H. Gan, Y. Yao, A. Aspuru-Guzik, Q. Y. Xu and D. Su, *ACS Nano*, 2019, **13**, 9421–9430.